J Mater Sci (2023) 58:7119–7135

Metals & corrosion

Micro- and nanostructure of additively manufactured, in-situ alloyed, magnetic spinodal $Fe_{54}Cr_{31}Co_{15}$

T. Mairhofer[1,*], S. Arneitz[3], F. Hofer[1,2], C. Sommitsch[3], and G. Kothleitner[1,2]

[1] Institute of Electron Microscopy and Nanoanalysis, Graz University of Technology, Steyrergasse 17, Graz 8010, Austria
[2] Graz Centre for Electron Microscopy, Steyrergasse 17, Graz 8010, Austria
[3] Institute of Materials Science, Joining and Forming, Graz University of Technology, Kopernikusgasse 24, Graz 8010, Austria

Received: 16 December 2022
Accepted: 28 March 2023
Published online: 19 April 2023

ABSTRACT

Exploring the chemical micro- and nanostructure of metal alloys is essential to understand their physical properties, such as magnetism or hardness. Additively manufactured (AM) materials, e.g. via laser powder bed fusion (LPBF) followed by various heat treatments, can raise further questions concerning the printed material. For the in-situ alloyed, spinodal $Fe_{54}Cr_{31}Co_{15}$ system, the macroscopic magnetic behaviour is greatly influenced by subsequent homogenisation and heat treatment steps. Here we show that the decomposition takes place on the nanometre scale, resulting in ferromagnetic FeCo-rich particles embedded in a Cr-rich matrix. By studying phenomena like chemical homogeneity, grain structure, and texture of the in-situ alloyed material at different scales, we reveal correlations between the heat treatment and the resulting nanostructure and its ferromagnetic properties. We found that the isothermal heating conditions determine the degree of phase segregation and that a homogenization step can be omitted for additively manufactured, in-situ alloyed FeCrCo alloys. The approach thereby offers insight and a path for also tailoring specific manufacturing parameters to provide the right quality printed materials with desired functionalities. For example, magnetic FeCrCo alloys are often used in electric motors or magnetic sensors, and the flexibility of the presented approach can lead to optimal use of the material.

Handling Editor: Megumi Kawasaki.

Address correspondence to E-mail: thomas.mairhofer@felmi-zfe.at

https://doi.org/10.1007/s10853-023-08445-z

Introduction

In recent years, additive manufacturing has been established not only as a method for the production of structural materials but also for functional materials design [1–3]. The method of laser powder bed fusion (LPBF) provides great freedom considering design, but usually, commercial powders suitable for additive manufacturing are limited to a few very common materials. To overcome this limitation, the method of in-situ alloying can provide the desired flexibility. In this technique, a mixture of elemental powders is used instead of the pre-alloyed powder. The main advantage here in comparison with using pre-alloyed powders is, first, that for additively manufactured (AM) novel materials, no pre-alloyed powder exists. Thereby, in-situ alloying of pure element powder mixtures is often the only method that can be used for these very diverse classes of materials. Second, the chemical composition of the alloy can be varied by simply changing the composition of the powder mixture. This may be crucially important for rapid prototype design, where adaption of the chemical composition might become necessary for research and development purposes. For example, in industry 4.0, using pre-alloyed powders for these custom prototypes may be too slow and expensive [4–6]. Third, AM is important due to its ability to produce complex-shaped parts as well as the possibility of anisotropic printing [7–11].

Changing the composition, shape, and structure of an alloy may lead to drastic changes in its physical properties. This is especially true for the Fe–Cr–Co system, where this flexibility can be quite interesting. In this system, the magnetic properties can be vastly different depending on the chemical composition, as Kaneko et al. have already shown in their studies [12]. In this field, for AM, it might be of particular interest to be able to adjust the magnetic properties according to each specific case. Despite the flexibility in the AM process itself, an additional way of manipulating the chemical microstructure and, thereby, the magnetic properties is to spinodally decompose the alloy after printing. Spinodal decomposition is a well-known phenomenon during that an alloy decomposes when heated and held within the miscibility gap [13–17]. For FeCrCo alloys, it is known that it decomposes into two distinct chemical phases, a FeCo-rich and a Cr-rich phase with the first one causing the alloy to become ferromagnetic [18–21]. Coupling the flexibility of the AM in-situ alloying process with the spinodal decomposition procedure offers great potential to manipulate and fine-tune the physical properties such as magnetism of such alloys.

An important question for in-situ alloying is the issue of the homogeneity of the printed parts. In a previous study, we have shown that the homogeneity of in-situ alloyed FeCrCo alloys depends on the laser power and energy density used during the printing process [22]. A laser power of 240 W with an energy density of 400 Jmm^{-2} was found to produce the most homogeneous and dense alloys. Usually, homogenisation treatments after printing are applied to ensure full homogeneity. In this study, we extend the question of homogeneity down to the nanometre range and compare the chemical and magnetic micro- and nanostructural properties of an as-printed and fully homogenised samples. Additionally, we investigate the influence of different spinodal decomposition conditions (i.e. different heat treatments after printing) on these properties.

We used scanning electron microscopy energy-dispersive X-ray spectroscopy (SEM–EDXS) and electron backscatter diffraction (EBSD) to determine the chemical structure at the micrometre scale and scanning transmission electron microscopy (STEM) imaging and spectroscopy techniques to measure it at the nanometre scale. STEM–EDXS and magnetic differential phase contrast (DPC)—STEM imaging have been applied to map the chemical and magnetic nanostructures of the different alloys, respectively.

Methods

Printing parameters and SEM-EBSD measurements

Based on our previous work, three samples were chosen for further analysis due to their intriguing combination of heat treatments and magnetic performances. In Table 1, the printing parameters, the postprocessing heating treatments, and the magnetic properties are reprinted.

The used laser power and energy density were the same for all three specimens; however, the homogenisation and heat treatment after printing was different. If a sample was homogenised, it was heated up to 1100 °C for one hour. The heat treatment

Table 1 Overview of the three additively manufactured, in-situ alloyed, magnetic spinodal FeCrCo alloys used in this study. Reprinted from Arneitz et al. [22]

Sample	Laser power/W	Energy density/Jmm^{-2}	Homogenisation	Heat treatment	$\mu_0 H_c$/kAm^{-1}	μ_0Mr/T	BH$_{max}$/kJm^{-3}
FeCrCo_1	240	400	No	640HT	22.29	0.42	0.08
FeCrCo_2	240	400	1100 °C	640HT	19.10	0.47	0.08
FeCrCo_3	240	400	1100 °C	510HT	0.80	0.10	0.08

labelled 640HT denotes heating of the alloy at 640 °C for 1 h, followed by cooling it down to 510 °C with a cooling rate of 26 °C h^{-1} and keeping the temperature for another hour. The procedure labelled 510HT kept the alloy at 510 °C for 50 h. The chosen heat treatments are based on the miscibility gap of FeCrCo alloys, and further details can be found elsewhere [12, 22, 23].

The samples were printed on an ORLAS Creator from Coherent, Germany. X-ray diffraction (XRD) measurements on these samples were performed and published in an earlier paper by Arneitz et al. [22]. For SEM/EBSD investigation, samples were cut along the three main directions, called x, y and z (see Fig. S.1 of the supplementary information), and embedded in a conductive resin. Samples were then ground using SiC paper (800, 1200, 2000 and 4000) for 3 min each, polished (3 and 1 µm) for 10 and 30 min, respectively, and vibropolished (0.01 µm) over night.

EBSD investigations with two degrees of resolution (overall image and close-up) were performed in a TESCAN REM—Mira electron microscope using TSL OIM Analysis v.8 software for analysis. A working distance of 25 mm and a field of view of 1000 × 800 µm for the overview images and 200 × 160 µm for the close-up images were used. The exposure times were set to 3.5 ms and 10 ms with step sizes of 0.85 µm and 0.1 µm, respectively. For the image processing, (1) static background division, (2) dynamic background division and (3) intensity histogram normalization were deployed.

Specimen preparation STEM

For (S)TEM measurements, thin slices were cut out of the 3D printed blocks. Disc-shaped specimens with diameters of roughly 3 mm were subsequently either punched or cut out. To achieve electron transparency, the specimens were mechanically thinned using a dimple grinder followed by Ar-ion milling under cryogenic conditions using a PIPS II from AMETEK Inc., USA.

STEM measurements

High-resolution imaging and spectroscopy were performed using a TFS Titan^3 G2 60–300 microscope (Thermo Fisher Scientific Inc., USA) in scanning TEM (STEM) mode operating at 300 kV acceleration voltage. STEM images were acquired with a high-angle annular dark field (HAADF) detector (collection angle of 63–200 mrad, Cameral length (CL) = 91 mm) using Velox software (Thermo Fisher Scientific [24]) for data acquisition and processing. Energy dispersive X-ray spectroscopy (EDXS) and elemental mapping were carried out with a TFS Super-X detector (Chemi-STEM technology, solid angle: 0.7 sr [25]) within the Titan microscope and Velox software was used for data acquisition and processing again. OriginLab (Version 2021b) was employed for plotting and statistical analysis of the quantified EDXS data.

LM-STEM DPC measurements

Mapping the in-plane magnetic domain structure was achieved by low-magnification STEM differential phase contrast (LM-STEM DPC) imaging. To obtain the magnetic structure, a 4-segment annular detector and Velox software were used. STEM DPC uses the interaction of the electron beam with the magnetic structure while passing through the specimen to map fields. Classically, the interaction between an electron and a magnetic or electric field is described by the Lorentz force $F_L = q(\boldsymbol{E} + (\boldsymbol{v} \times \boldsymbol{B}))$, displaying a deflection of the moving electron when passing through the field. By detecting the shift of the imaging electron beam of a STEM, the field structure causing the deflection can be detected and visualized. Thus, DPC is a powerful technique to determine the magnetic domain structure of spinodal FeCrCo alloys at the nanometre scale. More details about STEM

DPC and how it can be used to determine the magnetic domain structure of spinodal alloys can be found in a recent paper about spinodal $Cu_{52}Ni_{34}Fe_{14}$ [26] and in further literature [27–35].

To secure a low-field environment, the microscope was operated in low-magnification (LM) mode and the objective lens was switched off during DPC measurements leading to residual stray fields < 12 kAm^{-1}. Velox software was again used for DPC data acquisition and generating the difference and sum images. A MATLAB (Version R2019b) script was written to display a false-colour magnetic field structure, which we refer to as colour wheel representation. The processing workflow of getting from single quadrant images to the magnetic field structure in colours is illustrated in figure S.8 of the supplementary information.

Results and discussion

SEM–EDXS measurements

We begin the discussion of our results with a SEM–EDXS elemental map at the larger (µm) scale for Fe to elaborate the chemical homogeneity of the in-situ alloyed but unhomogenised FeCrCo_1 specimen. Figure 1 shows the grey-scaled Fe elemental map that reveals a rather homogeneous distribution of Fe across the scanned area. However, we also observe a few dark inclusions together with brighter and darker inhomogeneities. In order to quantify the homogeneity of the specimen we determined the amount of area covered either by brighter or darker features using the software Fiji (Version 2.3.0) [36]. There, the histogram of occurring grey values can be used to set certain thresholds and colourize and determine the brighter (Fe-richer) and darker (Fe-depleted) areas. The process was repeated several times to determine maximum values for the area fractions of the different inhomogeneities. The found results are displayed in image (b) for the Fe-rich areas and (c) for the Fe-depleted regions.

We found that more than 90% of the FeCrCo_1 alloy had a similar homogenous distribution of Fe, Cr and Co compared to the two other specimens that did not show chemical inhomogeneities after their additional heat treatment. The homogeneous distributions of Fe of specimens FeCrCo_2 and FeCrCo_3 are shown in figure S.2 in the supplementary information. However, roughly 3 percent of the investigated area showed a higher Fe content and ~ 6% showed either higher Co or Cr content. Similar elemental maps for Cr revealed that the very dark inclusions seen within image (a) are almost pure Cr-particles (> 98 at.% Cr) that probably stem from insufficient melting of larger Cr-powder particles. Cr has a higher melting point (1907 °C) compared to the other used powders (1538 °C for Fe and 1423 °C for CoCr). The residual inhomogeneous mixing is likely due to high cooling rates and complex melt pool temperature fields of the LPBF process [37, 38]. Interestingly, the two homogenised alloys did not show any differences at this level of resolution despite their different spinodal decomposition treatment that resulted in vastly different magnetic properties (e.g. coercivity, see Table 1).

To analyse the chemical composition, we also evaluated the EDXS elemental maps quantitatively for Fe, Cr and Co of all three specimens. The results are displayed in Fig. 2, where the Fe, Cr and Co content in at.% is shown for the nominal overall

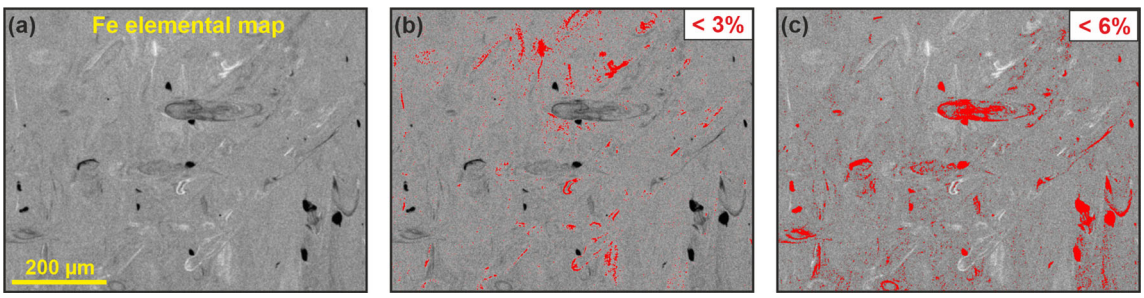

Figure 1 SEM–EDXS elemental map of Fe with a field of view of 850 × 600 µm (**a**). Images (**b**) and (**c**) highlight the Fe-rich and Fe-poor regions, respectively. The maximal area fraction coloured in red is displayed in the upper right corner of the images. For the displayed image **b** the threshold was set to 2.9%, meaning that the 2.9% brightest pixels were coloured. For image **c**, the threshold was at 5.1% for the darkest pixels.

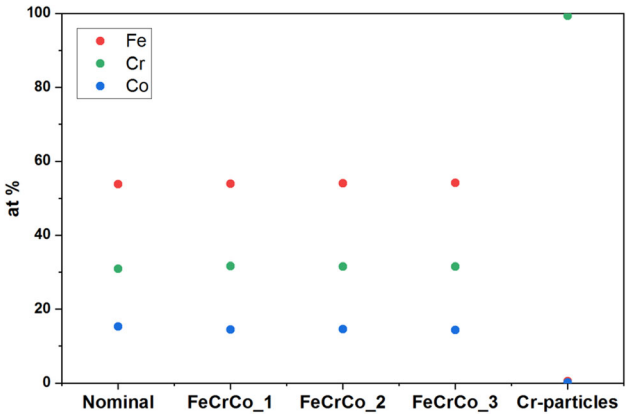

Figure 2 Quantitative analysis of the chemical composition of all three alloys and the Cr-rich inhomogeneities of FeCrCo_1. As a reference, the nominal composition is also displayed.

composition, all three alloys and the Cr-particles of FeCrCo_1 revealed in Fig. 1. The homogeneous parts of FeCrCo_1, FeCrCo_2 and FeCrCo_3 all showed similar compositions of (54.1 ± 0.4) at.% Fe, (31.6 ± 0.3) at.% Cr, and (14.4 ± 0.3) at.% Co, and thus were in good agreement with the nominal composition of $Fe_{53.8}Cr_{31.0}Co_{15.2}$. It should be noted that for the quantitative values displayed in Fig. 2, only the SEM–EDXS signals of Fe, Cr and Co were used, neglecting minor signals of Mn or Mo (between 0.5 and 1 at.% each) and others. This approach has also been used later for the STEM–EDXS analysis for better comparability. Errors were calculated assuming a t-distribution of the mean values for Fe, Cr and Co of the three alloys with a confidence interval of 95% ($\alpha = 0.05$, $t = 4.303$) [39].

The microscopic EDXS elemental maps reveal at least three interesting facts about the investigated samples. First, the homogenisation step during the heat treatment influences the chemical homogeneity. Second, with optimized printing and in-situ alloying parameters, a homogeneity > 90% is regularly achievable. This denotes progress in the field of in-situ alloying, since homogeneity is always a concern with this technique [7, 40–43]. Third, the spinodal decomposition takes place at the nanometre scale and the change of the chemical structure there cannot be detected with the conducted SEM–EDXS measurements.

EBSD analysis

In order to further understand the structure of the additively manufactured alloys at the larger (µm) scale, electron backscatter diffraction (EBSD) measurements were conducted. Figure 3 shows the inverse pole figure (IPF) maps of all three alloys measured along each main direction of the printed cubes, which is parallel to the building direction (i.e. top view along the *z*-direction) and perpendicular to it along x and *y* (side and front view), respectively.

Comparing the grain structures perpendicular and parallel to the growing direction, one major difference becomes evident. Grains in the *xy* plain (images a, d and g) appear more equiaxial, while grains in the *xz* (images b, e and h) and *yz* (images c, f and i) plane are larger and more columnar. This can also be seen when analysing the aspect ratios of the grains for each plane of orientation, plotted in figure S.3 in the supplementary information. This is probably due to the epitaxial growth of the grains, which is typically observed in the LPBF process [44–47]. The resulting larger and elongated grains parallel to the building direction and smaller, more equiaxial grains perpendicular to it, are also revealed, when comparing the grain size distribution for each direction, as shown in Fig. 4.

There, the grain size distribution perpendicular to the building direction, i.e. grain sizes measured from images (a), (d) and (g), is plotted in red and parallel to it are displayed in green and blue. For all three specimens the grain sizes are smaller perpendicular to the building direction. Additionally, larger grains (> 175 µm) appear only within the homogenised specimens FeCrCo_2 and FeCrCo_3. This is most likely due to the fact that upon homogenisation (high T), very small grains are eventually consumed by the surrounding grains resulting in a few larger ones.

This observation is also displayed in Table 2, where the three specimens' mean grain sizes along all three directions (*xy*, *xz*, and *yz*) are shown. For FeCrCo_1, the mean grain size parallel to the printing direction is just slightly bigger, whereas for FeCrCo_2 and FeCrCo_3, a significant shift towards a larger diameter is observed.

To further analyse the very small grains found only within FeCrCo_1, a magnified inverse pole figure map is displayed in figure S.4 in the supplementary information. The regions with a low confidence index showed smaller grains with a higher degree of misorientation. These areas probably formed due to the high cooling rates in the LPBF process and were only observed in the unhomogenised specimen [48]. However, comparing the

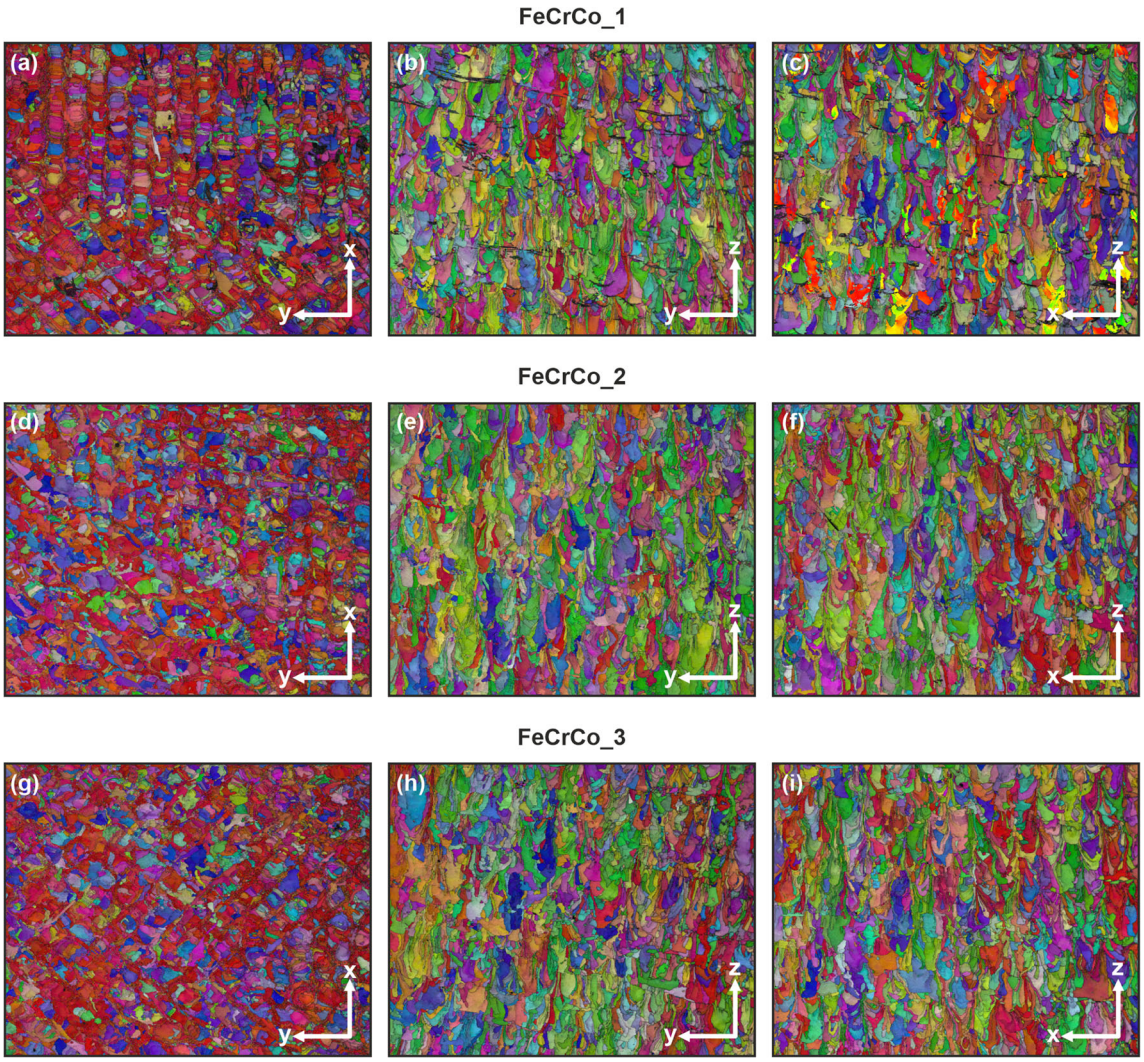

Figure 3 Inverse pole figure maps of FeCrCo_1 (**a-c**), FeCrCo_2 (**d-f**) and FeCrCo_3 (**g-i**) measured along the *z*-, *x*- and *y*-direction defined by figure S.1, respectively. The field of view for all images is 1000 × 800 µm.

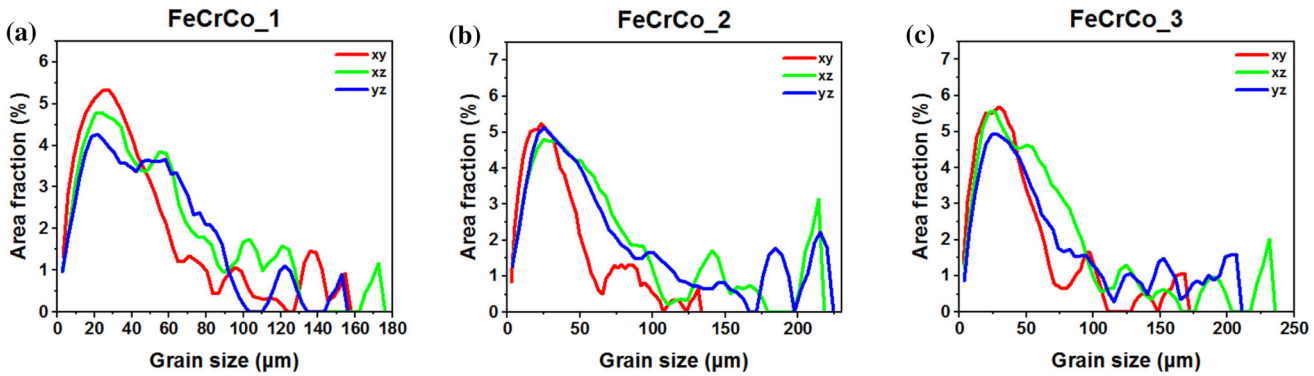

Figure 4 Grain size distribution perpendicular (red) and parallel (green, blue) to the building direction (*z*) of all three specimens.

Table 2 Evaluation of the mean grain size perpendicular (*xy*) and parallel (*xz* and *yz*) to the printing direction according to the distributions displayed in Fig. 4

Mean grain size	FeCrCo_1	FeCrCo_2	FeCrCo_3
*xy*_mean/µm	93	77	94
*xz*_mean/µm	108	144	136
*yz*_mean/µm	100	158	144

overall amount of misorientation for all three specimens, little quantitative differences can be found (see S.5). Another measure showing the similarities between all three alloys independent of their homogenisation and heat treatments is their strong < 001 > texture parallel to the building direction. Figure 5 displays the pole figure images recorded along the *z*-direction revealing the similar textures and that the *x*-, *y*- and *z*- printing directions can be identified as the [100], [010] and [001] directions, respectively, of the body-centred cubic (bcc) crystal structure.

Such an occurrence of a strong < 001 > texture parallel to the building direction is consistent with other studies on Fe-based materials [49–52]. The most prevalent < 001 > texture is found within FeCrCo_1, which can probably be attributed to a loss of texture during the homogenisation treatment. The slightly stronger texture may also be the reason for the higher coercivity of FeCrCo_1 compared to FeCrCo_2 (see Table 1).

Summarising the SEM–EDXS and EBSD results, we found that all three specimens are very similar in terms of grain structure, grain growth, texture, and chemical homogeneity at the larger scale (µm). The as-printed FeCrCo_1 displays some chemical inhomogeneities highlighted by Cr-particles and the strongest < 001 > texture parallel to the building direction. Other than that, only a few differences between unhomogenised and homogenised specimens were found. As a consequence, by in-situ alloying, the homogenisation step within the heat treatment may be omitted, and time and energy can be saved.

The two homogenised but differently spinodally decomposed alloys appear almost identical, although previous magnetic hysteresis measurements strongly suggest a different micro- or nanostructure. Therefore, a more detailed analysis at a higher resolution is mandatory to fully explore the similarities and differences of the chemical nanostructures and their influence on the magnetism of the alloys.

(S)TEM imaging

To gain a better understanding of the differences and similarities of the micro- and nanostructure of the different alloys, we employed high-resolution scanning transmission electron microscopy (HR—STEM) imaging and energy-dispersive X-ray spectroscopy. In a first step, high-angle annular dark field (HAADF) images were recorded. For a better comparison, all the alloys were tilted into

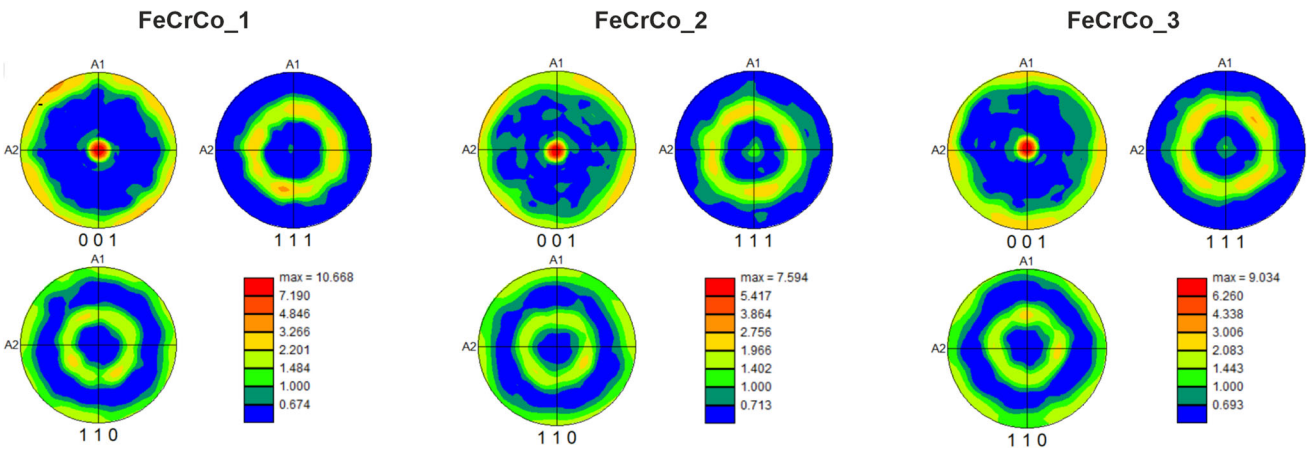

Figure 5 Pole figure images, showing the occurring textures in samples FeCrCo_1 (**a**), FeCrCo_2 (**b**) and FeCrCo_3 (**c**). All specimens were investigated along the z-direction, i.e. the texture of the cuts along the *xy* plane is recorded. A clear < 001 > texture can be seen in all three samples parallel to the building direction, with the unhomogenised sample (FeCrCo_1) having the strongest texture.

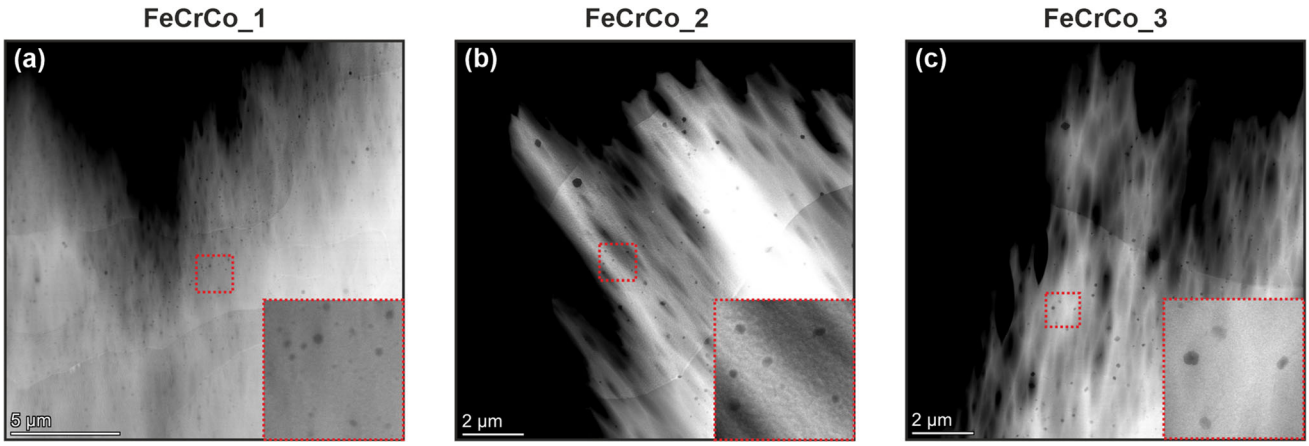

Figure 6 Large-area HAADF images of FeCrCo_1 (**a**), FeCrCo_2 (**b**) and FeCrCo_3 (**c**) displaying grain sizes and structures similar to SEM/EBSD measurements. Furthermore, randomly distributed dark inclusions can be seen within all three images.

a < 001 > crystallographic zone axis before acquiring the images. Selected area electron diffraction (SAED) and convergent beam electron diffraction (CBED) were used to secure proper alignment.

Figure 6 displays large area HAADF images of all three alloys and reveals similar grain sizes and structures compared to the previous SEM/EBSD findings. Additionally, small dark inclusions can be found randomly distributed across all three alloys. Larger zoom areas are marked with a red dashed rectangle and displayed in the lower right of the images to better visualize the dark inclusions. Slight changes in the brightness of different grains can be attributed to thickness variations across the regions of interest as well as tilting between the grains. Consequently, only one grain at a time was tilted into a < 001 > zone axis (ZA), moving others out of a perfect ZA alignment (typically a couple of degrees). Due to the clear < 001 > texture of all three alloys, a ZA alignment was easily achieved. The images of FeCrCo_2 and FeCrCo_3, Figs. 6b, c, respectively, also show several milling traces stemming from the ion bombardment during the thinning process. Nevertheless, on such larger scales, all three alloys display again very similar structures.

STEM—EDXS measurements of the nanostructure

To derive the chemical composition of the nanostructures, STEM–EDXS spectroscopy was carried out. A detailed overview of the chemical structures found for all three specimens is displayed in Fig. 7. The top row of images (a, c and e) reveals the HAADF images of the three specimens, the second row (b, d and f) the overlay of the Cr, Fe and Co EDXS elemental maps, respectively. The Cr signal is displayed in blue, the Fe signal in red and the Cr signal in green and additive colour mixing is used to display the overlay signals. The third row of images displays additional EDXS elemental maps/overlays of the same area for FeCrCo_1. The field of view for FeCrCo_1 and FeCrCo_2 is 750 nm × 750 nm, whereas for FeCrCo_3 it is 100 nm × 100 nm.

The HAADF images for FeCrCo_1 and FeCrCo_2 both display a similar structure of brighter particles embedded in a slightly darker matrix. Within each image, one dominant dark inclusion can also be seen. As mentioned earlier, both specimens are expected to spinodally decompose into FeCo-rich particles embedded in a Cr-rich matrix, and the HAADF images strongly support that. The contrast of HAADF images strongly depends on the average atomic number ($\sim Z^2$), meaning areas with heavier elements will appear brighter than areas containing light elements. Thus, the brighter particles are expected to contain more iron and cobalt ($Z_{Cr} = 24$, $Z_{Fe} = 26$, $Z_{Co} = 27$) than the darker surrounding matrix. The overlay of the EDXS elemental maps (b and d) validate this assumption, showing FeCo-rich particles (yellow) embedded in a Cr-rich matrix (blueish).

Single EDXS elemental maps for Fe, Cr and Co of all specimens are shown in figure S.6 of the supplemental information. The FeCo-rich particles appear in various shapes, trending however towards cubic and cuboid forms. Furthermore, the edges of the particles

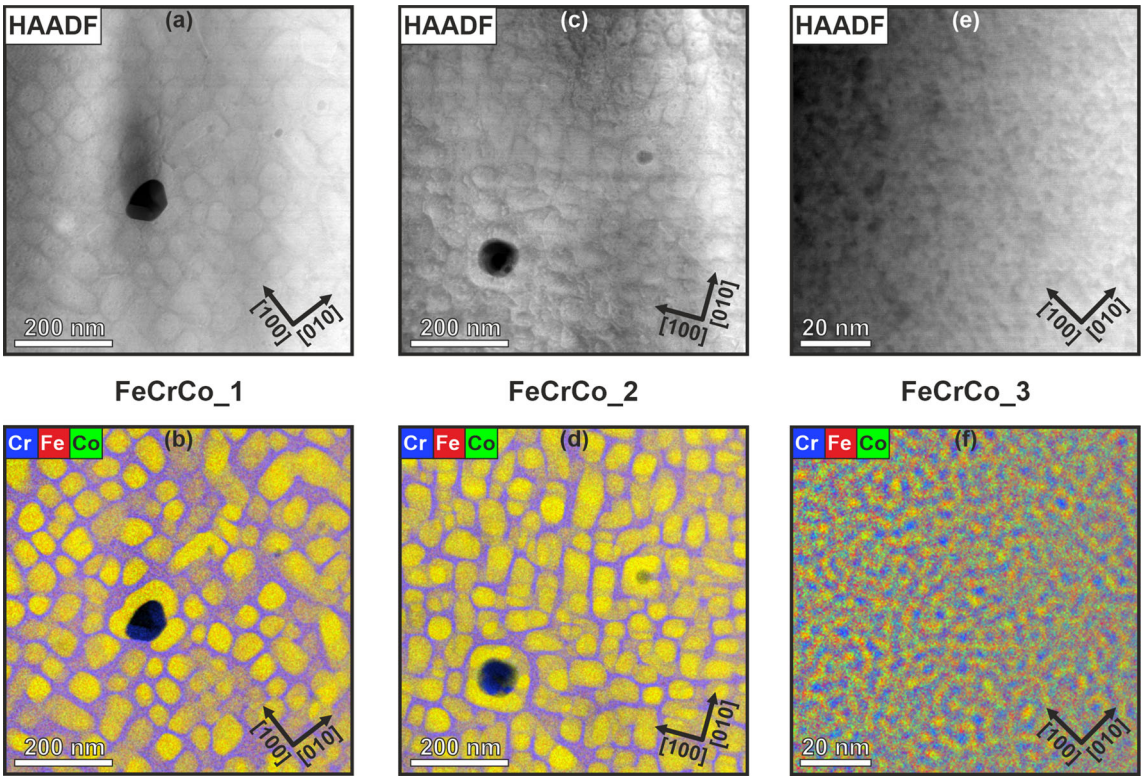

Figure 7 HAADF and overlays of Cr, Fe and Co EDXS elemental maps for all three alloys. The alignment along the [001] crystallographic direction is indicated by the black arrows in the lower right of each image for each alloy. The field of view of the images of FeCrCo_1 (images (**a**) and (**b**)) and FeCrCo_2 ((**c**) and (**d**)) is 750 nm × 750 nm, whereas for the images of FeCrCo_3 ((**e**) and (**f**)) it is 100 nm × 100 nm.

tend to align along the < 001 > crystallographic directions, as indicated by the dark arrows in the lower right of the images. The Cr-rich matrix also contains molybdenum which most likely originates from the Co29Cr6Mo-powder used for printing. The Mo EDXS elemental map is displayed in the image (a) of figure S.7. of the supplementary information.

Analysing the dark inclusion of FeCrCo_1, the EDXS analysis revealed an oxide particle containing Si, Al, Mn and O. It seems that the particle consists of an Al/Si richer core surrounded by Mn and covered by O. However, the particle is mainly covered by the FeCo-rich phase but otherwise does not seem to influence the decomposition of the FeCrCo alloy. An EDXS overlay image of the particle is shown in figure S.7 of the supplementary information. Similar oxide particles are found in all three alloys, suggesting that they emerge due to residual material within the printing chamber during printing or impurities within the powders used for printing. However, the authors are aware that in future measurements, special attention should be paid to the cleanliness of the printing chamber and the powder used in order to obtain the purest alloys.

Contrary to the previous two alloys, FeCrCo_3 exhibits a different nanostructure that is revealed by images (e) and (f). The HAADF image does not show the same particles-in-matrix structure even though small darker and brighter features can be seen. However, the EDXS elemental map reveals a granular-like structure consisting of small particles, either FeCo- or Cr-rich. The particles are considerably smaller, also reflected by the smaller scanned area of 100 nm × 100 nm. The change of the nanostructure towards a granular-like elemental distribution of Fe, Cr and Co of FeCrCo_3 is also displayed by the individual EDXS elemental maps shown in figure S.5 within the supplementary information.

A further comparison of the FeCo-rich particle sizes of the three alloys is given in Fig. 8. There, the average sizes of the particles are shown. Mean diameters of (69 ± 15) nm, (69 ± 18) nm and (5.7 ± 1.6) nm for FeCrCo_1, FeCrCo_2 and FeCrCo_3 are found.

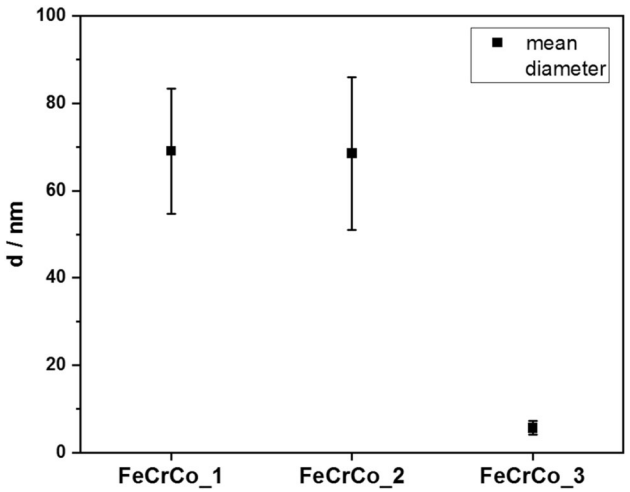

Figure 8 Mean diameter of FeCo-rich particles for all three specimens. The diameters were measured out of the overlays of EDXS elemental maps (Fig. 7).

This again displays the similarity of alloys FeCrCo_1 and FeCrCo_2 and the significant change of the microstructure for specimen FeCrCo_3. Aside from analysing the size of the FeCo-rich particles, also a quantitative analysis of the EDXS spectra, gathered from the elemental maps shown in Fig. 7, has been performed. The Cr, Fe and Co compositions for all three alloys and both the Cr-rich matrix and the FeCo-rich particles are displayed in Fig. 9.

The overall composition for all three alloys was found to be (54.2 ± 1.0) at.% Fe, (31.0 ± 0.6) at.% Cr and (14.8 ± 0.5) at.% Co, neglecting the other minor signals like Mo or from the oxide particles for simplicity. These values match very well with the results found with SEM–EDXS and the nominal composition $Fe_{53.8}Cr_{31.0}Co_{15.2}$.

For alloys FeCrCo_1 and FeCrCo_2, the Cr-rich matrix consists of (57.2 ± 2.1) at.% Cr, (36.2 ± 1.7) at.% Fe and (6.6 ± 0.6) at.% Co and the FeCo-rich particles of (8.3 ± 2.1) at.% Cr, (69.1 ± 1.4) at.% Fe and (22.6 ± 0.9) at.% Co. The compositions for alloy FeCrCo_3 are slightly different and shifted closer to the overall composition. This may be very well understood, considering the average size of the particles of FeCrCo_3 and the thickness of the sample. Although the thickness of the specimen was not determined experimentally, it is sufficient to assume a thickness multiple times the size of the FeCo-rich or Cr-rich particles. Hence, the quantified EDXS signal of a certain particle seen within the elemental map is not solely due to the single phase of that specific particle but a convolution of various signals of both phases. Thus, the EDXS signals of one phase/particle are expected to change towards the overall composition of the alloy, which is exactly what can be observed.

The values for the particle sizes as well as the compositions were gained by averaging the results of 10 line profiles/spectra for each specimen and phase. For the overall values, the results for the three specimens were averaged. The errors shown were calculated assuming a t-distribution and using a confidence interval of 95% ($\alpha = 0.05$ and $t = 2.262$ for the particles/matrix and $t = 4.303$ for the overall composition) [39]. The EDXS signals were quantified using standard Cliff-Lorimer quantification provided by Velox Software (theoretical k—factors). A Brown-

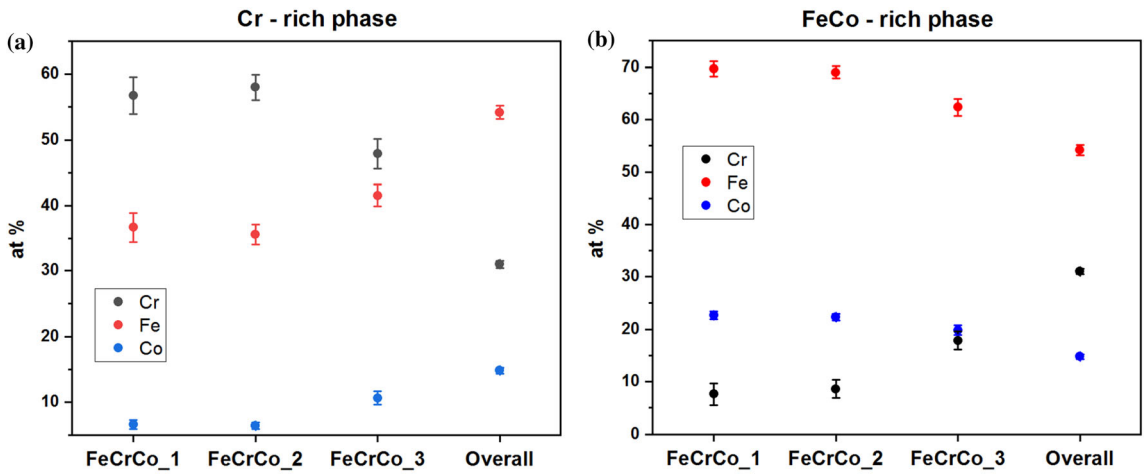

Figure 9 Quantitative STEM–EDXS analysis providing the chemical compositions of the Cr-rich (**a**) and FeCo-rich (**b**) phases as well as the overall composition for all three alloys.

Powell model for the ionization cross section model and no absorption correction was used [53, 54].

The nanostructures revealed by EDXS elemental mapping and quantification provide a few interesting insights. First, comparing the results for alloy FeCrCo_1 and FeCrCo_2, one can clearly state that both structures are strikingly similar despite the missing of a homogenisation step of FeCrCo_1 before the heat treatment. Although the SEM–EDXS measurements showed less homogeneity of the alloy FeCrCo_1, the STEM analysis revealed a similar nanostructure of both alloys when comparing a homogeneous region of FeCrCo_1 with FeCrCo_2. We can therefore conclude that the heat treatment after a possible homogenisation, i.e. the spinodal decomposition of the alloy, is the main reason for the evolution of the nanostructure into FeCo-rich particles embedded in a Cr-rich matrix. Comparing the results for FeCrCo_1 and FeCrCo_2, it is safe to state that the as-printed alloy was sufficiently homogeneous to provide a similar micro- and nanostructure with the benefit of saving time and energy by omitting the homogenisation step. Combining this with the flexibility of using pure element powders for printing, the process provides tremendous upsides for future material designs and applications.

Second, the difference in the nanostructure between FeCrCo_1/FeCrCo_2 and FeCrCo_3 is obvious. This further strengthens the statement from above that the heat treatment is the main reason for the evolution of the nanostructure. This is known for spinodally decomposed alloys; however, for magnetic alloys like FeCrCo, the change of the micro- and nanostructure also affects its magnetic properties [55–57]. This is also reflected by the magnetic hysteresis measurements presented before, showing that the formation of FeCo-rich particles is the reason for the FeCrCo alloy to become ferromagnetic. Depending on the size of these ferromagnetic particles, the interaction of these changes, and therefore also the macroscopic magnetic properties. Due to the similar micro- and nanostructure, FeCrCo_1 and FeCrCo_2 display similar coercivities and remanence magnetizations, whereas FeCrCo_3 possesses a coercivity two magnitudes smaller. This can be explained by the change of the nanostructure from larger FeCo particles in a Cr-rich matrix for FeCrCo_1 and FeCrCo_2 to a granular-like structure that has only smaller FeCo-rich particles present within FeCrCo_3. Thus, depending on the heat treatment, not only the chemical nanostructure but also the magnetism of FeCrCo alloys can be tuned.

Magnetic nanostructure

To investigate the magnetic nanostructures of alloys FeCrCo_1 and FeCrCo_2, we also conducted LM-STEM DPC investigations. Prior to DPC measurements, the objective lens of the microscope ($\sim$ 2 T field strength) was used to magnetize the alloy. Afterwards, the lens was switched off to secure a low-field environment with residual stray fields below 12 kAm^{-1}. Since the coercivities of the alloys were measured at 22.29 kAm^{-1} and 19.10 kAm^{-1}, respectively, the magnetic domain structure is hardly perturbed during measurements and can be mapped using LM-STEM DPC. Conversely, the magnetic structure of alloy FeCrCo_3 could not be determined since the coercivity of this alloy was too low (0.8 kAm^{-1}) to withstand the stray fields within the microscope. Again, this reflects the dramatic effect the different heat treatment has on the magnetism resulting from the different nanostructure.

Figure 10 displays an annular bright-field image and a magnetic DPC image of alloy FeCrCo_1 (a, b) together with the known overlay of the Cr, Fe and Co EDXS elemental maps of alloy FeCrCo_2 (c) as well as a magnetic DPC image (d) of the very same region. The DPC images exhibit the in-plane magnetic structures and are shown in colour wheel representation. There, the direction of the in-plane magnetic induction vector is imaged as a function of hue, and the colour wheel in the upper right reveals this correlation. Hence, the magnetic DPC images reveal the colourized in-plane magnetic domain structures [27].

Image (a) of Fig. 10 displays the sum image of all four DPC quadrants and thus is similar to an annular bright-field (ABF) image of the investigated region of FeCrCo_1. This can be helpful for identifying features within a DPC image stemming from dynamical scattering effects, such as bending contours which are nicely visible within BF-images. In order to minimize such effects, the alloy was again slightly tilted out of a perfect $< 001 >$ ZA alignment, resulting in a rather homogeneously grey BF image.

Nevertheless, a thickness gradient from the upper left to the lower right can be identified. The magnetic structure revealed by the DPC image (b) reveals a lamellar like domain structure (i.e. regions with different colours). Dark arrows within the DPC image

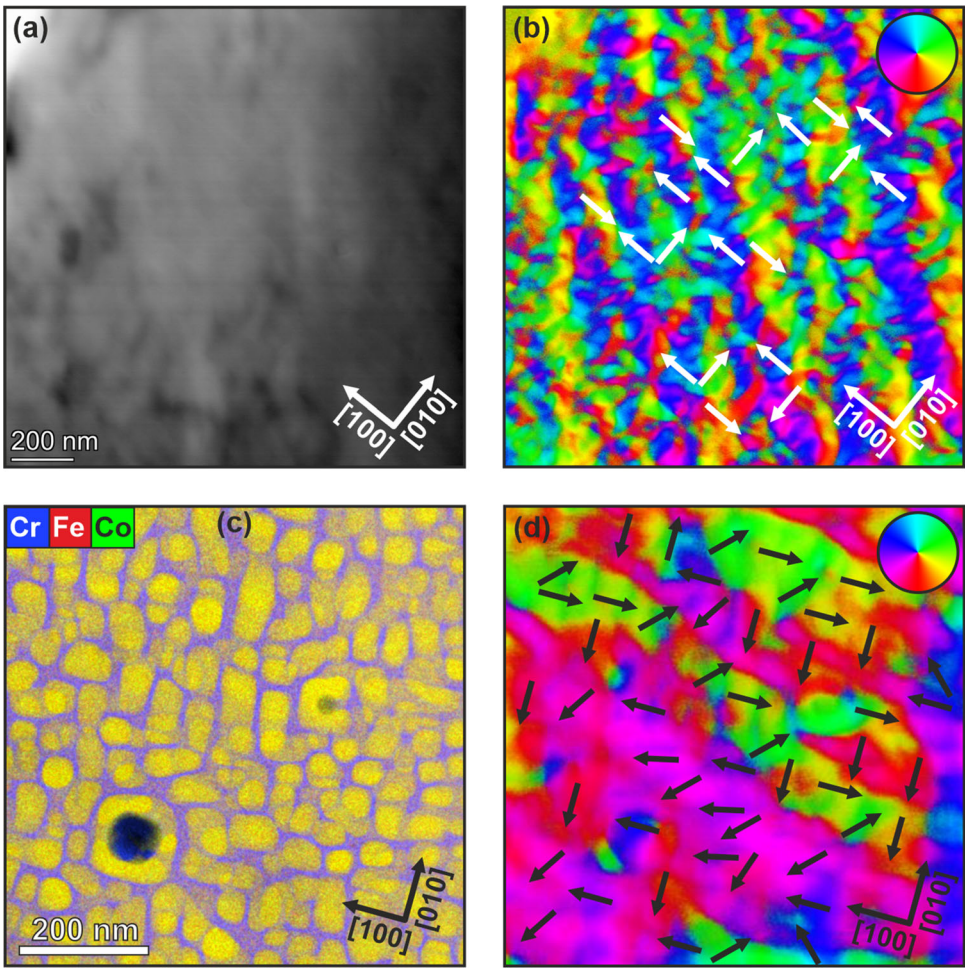

Figure 10 Images (**a**) and (**b**) show a bright-field and magnetic DPC image of FeCrCo_1. Additionally, an overlay of Cr, Fe and Co EDXS elemental maps (**c**) and a magnetic DPC image revealing the in-plane magnetic induction map (**d**) of the same area of FeCrCo_2 are displayed. The DPC images show the direction of the magnetization vectors as a function of hue. The colour wheel inset in the upper right exhibits the correlation between colour and direction of magnetization.

reveal the direction of the magnetic vector of certain areas, i.e. the magnetic domains. The arrows indicate a complicated pattern of magnetic domains with a tendency of the magnetization vector pointing roughly along the $< 100 >$ crystallographic directions. This is in accordance with the literature that postulates $< 100 >$ as the magnetic easy axes for Fe-rich FeCo [13]. However, a precise determination of the directions with respect to the crystallographic lattice is difficult since the specimen has been tilted out of an ideal [001] ZA alignment ($\sim 10°$) prior to the DPC measurements to minimize the before mentioned dynamical scattering effects [58, 59]. Nevertheless, a pattern of magnetic domains responsible for the magnetic behaviour of the alloy is clearly visible.

For alloy FeCrCo_2, the domain boundaries run roughly across the diagonal of the image from the upper left to the lower right. Again, dark arrows within the image illustrate the direction the magnetic induction vector is pointing to within certain regions. A similar tendency of the magnetic vector pointing along the $< 001 >$ crystallographic directions can be identified, further displaying the similarities of both alloys FeCrCo_1 and FeCrCo_2. Moreover, a comparison with the EDXS elemental map displays the coupling of several FeCo-rich particles to form one magnetic domain. Some magnetic domains are found to be significantly bigger than the FeCo particles, indicating that single domain FeCo-rich particles coupled to each other, forming one domain. Finally, only a weak correlation between the chemical and magnetic structure is observed since no preferred direction for the domain walls with respect to the chemical- and crystal structure was found.

One question that still remains is how different heat treatments and the resulting smaller or larger FeCo-rich particles affect the magnetic domain structure. Our measurements confirm that the size (and shape) of the FeCo-rich particles is directly

related to the magnetic hardness of the alloy. Other studies on spinodal FeCrCo alloys paint a very similar picture [23, 60]. There is also the possibility to predetermine the preferred magnetic direction by precipitating the alloy in a magnetic field or by mechanical deformation [18, 19, 61, 62]. It seems that by a clever choice of heat treatment parameters (temperature, treatment time, magnetic field) one can manipulate the chemical nanostructure in such a way that one can obtain well-defined (macroscopic) magnetic properties. Further high-resolution measurements of the nanostructure and its coupling with the magnetic domain structure are therefore needed to fully understand this relationship.

Summarising the results of this study, we found that regardless of homogenisation or spinodal decomposition parameters, all three investigated FeCrCo alloys were surprisingly similar at the larger µm scale. At the nanoscale, however, the differences became evident. Homogenisation prior to spinodal decomposition has only minor influences on the chemical nanostructure, which is illustrated by the similar EDXS elemental maps for FeCrCo_1 and FeCrCo_2. This is also reflected in terms of similar magnetic properties since both alloys exhibit comparable coercivities, remanences and magnetic domain structures revealed by LM-STEM DPC measurements. FeCrCo_3, on the other hand, showed a vastly different chemical nanostructure, which we conclude to be the reason for the change in magnetic properties.

This study shows the tremendous flexibility and freedom additive manufactured in-situ alloying processes can have. However, we also found that the spinodal decomposition process is the reason for these alloys to become ferromagnetic once the homogeneous base material is produced. In a further step, inhomogeneous/anisotropic printing, meaning printing different compositions at different regions, may open a multitude of new possibilities for printing mechanical, chemical and physical properties of an alloy. For the system FeCrCo, one can think of directly printing regions with higher or lower FeCo-contents to change the magnetic properties of the alloy and induce magnetic anisotropy. Another example would be a possible change in the mechanical hardness depending on the printing profile of different chemical compositions. Different heat treatment adds further flexibility, and so the AM and in-situ alloying process exhibits astonishing possibilities for future material designs. This new flexibility can help optimize devices and applications that use such magnetic alloys, such as electric motors or sensors [18, 23, 63–65].

Conclusion

The study explores the micro- and nanostructure of three additive manufactured spinodally decomposed magnetic FeCrCo alloys. The alloys were manufactured by laser powder bed fusion by in-situ alloying directly within the powder bed. We altered the heat treatment of the alloys to explore the influence of homogenisation and spinodal decomposition temperature on the chemical micro- and nanostructure and the resulting magnetic properties. The following conclusions can be drawn.

1) The grain structure of all three alloys was very similar and displayed elongated and larger grains parallel to the printing direction compared to more equiaxial appearances perpendicular to it.
2) SEM–EDXS elemental mapping exhibits very homogeneous distributions of Fe, Cr and Co for the homogenised specimens, whereas the as-printed alloy showed some inhomogeneities, such as Cr-rich particles within an otherwise homogeneous (> 90%) alloy.
3) For all three samples, a strong < 001 > texture was observed parallel to the building direction, which is consistent with findings from other studies.
4) STEM–EDXS elemental mapping at the nanoscale revealed the spinodal decomposition of all three alloys, i.e. the segregation of FeCo-rich particles within a Cr-rich matrix, causing the alloys to become ferromagnetic. The 640HT treatment led to (69 ± 15) nm large cuboid FeCo particles for both the as-printed and the homogenised alloy. The cuboid particles tend to align along the < 100 > crystallographic directions and cause the alloys to become magnetically hard. Decomposition at 510 °C resulted in a granular-like structure with much smaller FeCo-rich particles of (5.7 ± 1.6) nm, which explains the change of the macroscopic magnetic properties. Additionally, all alloys

possessed oxide particles containing Si, Al and Mn stemming from the printing process.

5) Mapping the in-plane magnetic induction of FeCrCo_1 and FeCrCo_2 with DPC-STEM showed again their similarities and that the appearance of FeCo-rich particles caused a complex pattern of elongated ferromagnetic domains.

Our study shows that combining in-situ alloying and spinodal decomposition of additively manufactured FeCrCo alloys provides unique flexibility to change and manipulate the chemical micro- and nanostructure. By doing that, physical properties such as the coercivity, remanence or mechanical hardness of the alloy can be changed and fine-tuned. Fully understanding the structure–property relationship at different scales is the key to intelligent future materials design and to directly produce materials with desired functionalities.

Acknowledgements

The authors want to thank Martina Dienstleder for (S)TEM specimen preparation and Georg Haberfehlner, Daniel Knez, Judith Lammer and Manfred Nachtnebel for helpful discussions. This project has received funding from the European Union's Horizon 2020 Research and Innovation Program under grant agreement No. 823717-ESTEEM3.

Author contributions

TM: conceptualization, investigation ((S)TEM), formal analysis, writing—original draft, writing—review & editing. SA: conceptualization, investigation (LPBF, SEM, EBSD), formal analysis, writing—original draft, writing—review & editing. FH: supervision, writing—review & editing. CS: writing—review & editing. GK: supervision, writing—review & editing.

Funding

Open access funding provided by Graz University of Technology.

Data availability

Data and code will be made available on request.

Declarations

Conflict of interest The authors declare that they have no known competing financial interests or personal relationships that could have appeared to influence the work reported in this paper.

Ethical approval Not applicable.

Supplementary information The supplementary information contains of a sketch of the printed cuboids, additional SEM EDXS elemental maps of FeCrCo_2 and FeCrCo_3, grain aspect ratio evaluations, a magnified IPF map of FeCrCo_1 together with a confidence index map and a kernel average misorientation (KAM) map, KAM evaluations of all three specimens, additional single element (Fe, Cr and Co) STEM EDXS elemental maps, STEM EDXS elemental maps of the oxide particle, and a description of the STEM DPC processing workflow.

Supplementary Information: The online version contains supplementary material available at https://doi.org/10.1007/s10853-023-08445-z.

References

[1] Rasiya G, Shukla A, Saran K (2021) Additive manufacturing-a review. Mater Today Proc 47:6896–6901. https://doi.org/10.1016/j.matpr.2021.05.181

[2] Ngo TD, Kashani A, Imbalzano G, Nguyen KTQ, Hui D (2018) Additive manufacturing (3D printing): a review of materials, methods, applications and challenges. Compos Part B Eng 143:172–196. https://doi.org/10.1016/j.compositesb.2018.02.012

[3] Wong KV, Hernandez A (2012) A review of additive manufacturing. ISRN Mech Eng 2012:1–10. https://doi.org/10.5402/2012/208760

[4] Sing SL, Yeong WY (2020) Laser powder bed fusion for metal additive manufacturing: perspectives on recent developments. Virtual Phys Prototyp 15:359–370. https://doi.org/10.1080/17452759.2020.1779999

[5] Sun S, Brandt M, Easton M (2017) Powder bed fusion processes. In: Brandt Milan (ed) Laser additive manufacturing. Elsevier, Amsterdam, pp 55–77

[6] Khorasani A, Gibson I, Veetil JK, Ghasemi AH (2020) A review of technological improvements in laser-based powder bed fusion of metal printers. Int J Adv Manuf Technol 108:191–209. https://doi.org/10.1007/s00170-020-05361-3

[7] Mosallanejad MH, Niroumand B, Aversa A, Saboori A (2021) In-situ alloying in laser-based additive manufacturing processes: a critical review. J Alloys Compd 872:159567. https://doi.org/10.1016/j.jallcom.2021.159567

[8] Askari M, Hutchins DA, Thomas PJ, Astolfi L, Watson RL, Abdi M, Ricci M, Laureti S, Nie L, Freear S, Wildman R, Tuck C, Clarke M, Woods E, Clare AT (2020) Additive manufacturing of metamaterials: a review. Addit Manuf 36:101562. https://doi.org/10.1016/j.addma.2020.101562

[9] Shoji Aota L, Bajaj P, Zschommler Sandim HR, Aimé Jägle E (2020) Laser Powder-Bed fusion as an alloy development tool: parameter selection for in-situ alloying using elemental powders. Materials 13:3922. https://doi.org/10.3390/ma13183922

[10] Zou R, Xia Y, Liu S, Hu P, Hou W, Hu Q, Shan C (2016) Isotropic and anisotropic elasticity and yielding of 3D printed material. Compos Part B Eng 99:506–513. https://doi.org/10.1016/j.compositesb.2016.06.009

[11] Zhang C, Li X, Jiang L, Tang D, Xu H, Zhao P, Fu J, Zhou Q, Chen Y (2021) 3D printing of functional magnetic materials: from design to applications. Adv Funct Mater 31:2102777. https://doi.org/10.1002/adfm.202102777

[12] Kaneko H, Homma M, Nakamura K, Okada M, Thomas G (1977) Phase diagram of Fe–Cr–Co permanent magnet system. IEEE Trans Magn 13:1325–1327. https://doi.org/10.1109/TMAG.1977.1059557

[13] Getzlaff M (2008) Fundamentals of magnetism. Springer-Verlag, Berlin Heidelberg

[14] Findik F (2012) Improvements in spinodal alloys from past to present. Mater Des 42:131–146. https://doi.org/10.1016/j.matdes.2012.05.039

[15] Cahn JW (1961) On spinodal decomposition. Acta Metall 9:795–801. https://doi.org/10.1016/0001-6160(61)90182-1

[16] Soriano-Vargas O, Avila-Davila EO, Lopez-Hirata VM, Dorantes-Rosales HJ, Gonzalez-Velazquez JL (2009) Spinodal decomposition in an fe-32 at.%Cr alloy during isothermal aging. Mater Trans 50:1753–1757. https://doi.org/10.2320/matertrans.M2009029

[17] Avila-Davila EO, Melo-Maximo DV, Lopez-Hirata VM, Soriano-Vargas O, Saucedo-Muñoz ML, Gonzalez-Velazquez JL (2009) Microstructural simulation in spinodally-decomposed Cu–70 at.%Ni and Cu–46 at.%Ni–4 at.%Fe alloys. Mater Charact 60:560–567. https://doi.org/10.1016/j.matchar.2009.01.003

[18] Xiang Z, Zhang L, Xin Y, An B, Niu R, Mardani M, Siegrist T, Lu J, Goddard RE, Man T, Wang E, Han K (2021) Ultrafine microstructure and hardness in Fe-Cr-Co alloy induced by spinodal decomposition under magnetic field. Mater Des 199:109383. https://doi.org/10.1016/j.matdes.2020.109383

[19] Zhang L, Xiang Z, Li X, Wang E (2018) Spinodal decomposition in Fe-25Cr-12Co alloys under the influence of high magnetic field and the effect of grain boundary. Nanomater Basel Switz 8:578. https://doi.org/10.3390/nano8080578

[20] Zhu F, Haasen P, Wagner R (1986) An atom probe study of the decomposition of Fe–Cr–Co permanent magnet alloys. Acta Metall 34:457–463. https://doi.org/10.1016/0001-6160(86)90081-7

[21] Sugimoto S, Satoh H, Okada M, Homma M (1991) The development of lt;100 gt; texture in Fe-Cr-Co-Mo permanent magnet alloys. IEEE Trans Magn 27:3412–3419. https://doi.org/10.1109/20.79083

[22] Arneitz S, Buzolin R, Rivoirard S, Sommitsch C (2022) Additive manufacturing of an Fe–Cr–Co permanent magnet alloy with a novel approach of in-situ alloying. Eur J Mater 2:475–497. https://doi.org/10.1080/26889277.2022.2098832

[23] Xiang Z, Zhang L, An B, Lu J, Niu R, Xin Y, Mardani M, Siegrist T, Goddard RE, Man T, Wang T, Wang E, Han K (2023) Effect of evolution of spinodal decomposition on microstructure and properties in multi-step aged FeCrCo alloy. Mater Charact 199:112764. https://doi.org/10.1016/j.matchar.2023.112764

[24] Thermo Fisher Scientific, Velox (n.d.) https://assets.thermofisher.com/TFS-Assets/MSD/Datasheets/velox-datasheet.pdf. Accessed Nov 28 2022

[25] Thermo Fisher Scientific, ChemiSTEM Technology: A revolution in EDX analytics, (n.d.). https://assets.thermofisher.com/TFS-Assets/MSD/Application-Notes/ChemiSTEM-Application-Brochure.pdf. Accessed Nov 28 2022

[26] Radlinger T, Winkler R, Knoll P, Zweck J, Plank H, Hofer F, Kothleitner G (2022) A study on the correlation between micro and magnetic domain structure of $Cu_{52}Ni_{34}Fe_{14}$ spinodal alloys. J. Alloys Compd 922:166214. https://doi.org/10.1016/j.jallcom.2022.166214

[27] Zweck J (2016) Imaging of magnetic and electric fields by electron microscopy. J Phys Condens Matter Inst Phys J 28:403001. https://doi.org/10.1088/0953-8984/28/40/403001

[28] Lubk A, Zweck J (2015) Differential phase contrast: an integral perspective. Phys Rev A 91:416. https://doi.org/10.1103/PhysRevA.91.023805

[29] Shibata N, Findlay SD, Matsumoto T, Kohno Y, Seki T, Sánchez-Santolino G, Ikuhara Y (2017) Direct visualization of local electromagnetic field structures by scanning transmission electron microscopy. Acc Chem Res 50:1502–1512. https://doi.org/10.1021/acs.accounts.7b00123

[30] Chapman JN, Batson PE, Waddell EM, Ferrier RP (1978) The direct Determination of magnetic domain wall profiles by differential phase contrast electron microscopy. Ultramicroscopy 3:203–214

[31] Rose H (1974) Phase contrast in scanning transmission electron microscopy. Optik 39:416–436

[32] Müller K, Krause FF, Béché A, Schowalter M, Galioit V, Löffler S, Verbeeck J, Zweck J, Schattschneider P, Rosenauer A (2014) Atomic electric fields revealed by a quantum mechanical approach to electron picodiffraction. Nat Commun 5:5653. https://doi.org/10.1038/ncomms6653

[33] Lazić I, Bosch EGT, Lazar S (2016) Phase contrast STEM for thin samples: Integrated differential phase contrast. Ultramicroscopy 160:265–280. https://doi.org/10.1016/j.ultramic.2015.10.011

[34] Campanini M, Erni R, Rossell MD (2019) Probing local order in multiferroics by transmission electron microscopy. Phys Sci Rev 5:237. https://doi.org/10.1515/psr-2019-0068

[35] Zweck J, Schwarzhuber F, Wild J, Galioit V (2016) On detector linearity and precision of beam shift detection for quantitative differential phase contrast applications. Ultramicroscopy 168:53–64. https://doi.org/10.1016/j.ultramic.2016.05.007

[36] Schindelin J, Arganda-Carreras I, Frise E, Kaynig V, Longair M, Pietzsch T, Preibisch S, Rueden C, Saalfeld S, Schmid B, Tinevez J-Y, White DJ, Hartenstein V, Eliceiri K, Tomancak P, Cardona A (2012) Fiji: an open-source platform for biological-image analysis. Nat Methods 9:676–682. https://doi.org/10.1038/nmeth.2019

[37] Hooper PA (2018) Melt pool temperature and cooling rates in laser powder bed fusion. Addit Manuf 22:548–559. https://doi.org/10.1016/j.addma.2018.05.032

[38] Thampy V, Fong AY, Calta NP, Wang J, Martin AA, Depond PJ, Kiss AM, Guss G, Xing Q, Ott RT, van Buuren A, Toney MF, Weker JN, Kramer MJ, Matthews MJ, Tassone CJ, Stone KH (2020) Subsurface cooling rates and microstructural response during laser based metal additive manufacturing. Sci Rep 10:1981. https://doi.org/10.1038/s41598-020-58598-z

[39] Hahn GJ, Hendrickson RW (1971) A table of percentage points of the distribution of the largest absolute value of k Student t variates and its applications. Biometrika 58:323–332. https://doi.org/10.1093/biomet/58.2.323

[40] Simonelli M, Aboulkhair NT, Cohen P, Murray JW, Clare AT, Tuck C, Hague RJM (2018) A comparison of Ti-6Al-4V in-situ alloying in selective laser melting using simply-mixed and satellited powder blend feedstocks. Mater Charact 143:118–126. https://doi.org/10.1016/j.matchar.2018.05.039

[41] Wang C, Tan XP, Du Z, Chandra S, Sun Z, Lim CWJ, Tor SB, Lim CS, Wong CH (2019) Additive manufacturing of NiTi shape memory alloys using pre-mixed powders. J Mater Process Technol 271:152–161. https://doi.org/10.1016/j.jmatprotec.2019.03.025

[42] Knieps MS, Reynolds WJ, Dejaune J, Clare AT, Evirgen A (2021) In-situ alloying in powder bed fusion: The role of powder morphology. Mater. Sci. Eng. A. 807:140849. https://doi.org/10.1016/j.msea.2021.140849

[43] Huber F, Rasch M, Schmidt M (2021) Laser powder bed fusion (PBF-LB/M) process strategies for in-situ alloy formation with high-melting elements. Metals 11:336. https://doi.org/10.3390/met11020336

[44] Chen ZW, Phan MAL, Darvish K (2017) Grain growth during selective laser melting of a Co–Cr–Mo alloy. J Mater Sci 52:7415–7427. https://doi.org/10.1007/s10853-017-0975-z

[45] Darvish K, Chen ZW, Phan MAL, Pasang T (2018) Selective laser melting of Co-29Cr-6Mo alloy with laser power 180–360W: cellular growth, intercellular spacing and the related thermal condition. Mater Charact 135:183–191. https://doi.org/10.1016/j.matchar.2017.11.042

[46] Nagase T, Hori T, Todai M, Sun S-H, Nakano T (2019) Additive manufacturing of dense components in beta-titanium alloys with crystallographic texture from a mixture of pure metallic element powders. Mater Des 173:107771. https://doi.org/10.1016/j.matdes.2019.107771

[47] Dadbakhsh S, Vrancken B, Kruth J-P, Luyten J, Van Humbeeck J (2016) Texture and anisotropy in selective laser melting of NiTi alloy. Mater Sci Eng A 650:225–232. https://doi.org/10.1016/j.msea.2015.10.032

[48] Qiu C, Chen H, Liu Q, Yue S, Wang H (2019) On the solidification behaviour and cracking origin of a nickel-based superalloy during selective laser melting. Mater Charact 148:330–344. https://doi.org/10.1016/j.matchar.2018.12.032

[49] Layer-wise engineering of grain orientation (LEGO) in laser powder bed fusion of stainless steel 316L | Elsevier Enhanced Reader (n.d.) https://doi.org/10.1016/j.addma.2020.101809

[50] Andreau O, Koutiri I, Peyre P, Penot J-D, Saintier N, Pessard E, De Terris T, Dupuy C, Baudin T (2019) Texture control of 316L parts by modulation of the melt pool morphology in selective laser melting. J Mater Process Technol 264:21–31. https://doi.org/10.1016/j.jmatprotec.2018.08.049

[51] Marattukalam JJ, Karlsson D, Pacheco V, Beran P, Wiklund U, Jansson U, Hjörvarsson B, Sahlberg M (2020) The effect of laser scanning strategies on texture, mechanical properties, and site-specific grain orientation in selective laser melted 316L SS. Mater Des 193:108852. https://doi.org/10.1016/j.matdes.2020.108852

[52] Sun S-H, Ishimoto T, Hagihara K, Tsutsumi Y, Hanawa T, Nakano T (2019) Excellent mechanical and corrosion properties of austenitic stainless steel with a unique crystallographic lamellar microstructure via selective laser melting. Scr Mater 159:89–93. https://doi.org/10.1016/j.scriptamat.2018.09.017

[53] Cliff G, Lorimer GW (1975) The quantitative analysis of thin specimens. J Microsc 103:203–207. https://doi.org/10.1111/j.1365-2818.1975.tb03895.x

[54] Powell CJ (1976) Cross sections for ionization of inner-shell electrons by electrons. Rev Mod Phys 48:33–47. https://doi.org/10.1103/RevModPhys.48.33

[55] Kashyap I, Vetter EP, Floro JA, Graef M (2019) Lorentz TEM study of the magnetic microstructure in near-eutectoid Co-Pt alloys. J Magn Magn Mater 479:204–211. https://doi.org/10.1016/j.jmmm.2019.02.036

[56] Joffe I, Gaunt P (1971) Magnetic hardening and phase segregation in CuNiFe and CuNiCo alloys. J Phys Appl Phys 4:586

[57] Kim J-S, Takeda M, Bae D-S (2016) Microstructural evolution and magnetic properties of ultrafine solute-atom particles formed in a Cu 75 –Ni 20 –Fe 5 alloy on isothermal annealing. Jpn J Appl Phys 55:123002. https://doi.org/10.7567/JJAP.55.123002

[58] Mawson T, Nakamura A, Petersen TC, Shibata N, Sasaki H, Paganin DM, Morgan MJ, Findlay SD (2020) Suppressing dynamical diffraction artefacts in differential phase contrast scanning transmission electron microscopy of long-range electromagnetic fields via precession. Ultramicroscopy 219:113097. https://doi.org/10.1016/j.ultramic.2020.113097

[59] Shibata N, Findlay SD, Sasaki H, Matsumoto T, Sawada H, Kohno Y, Otomo S, Minato R, Ikuhara Y (2015) Imaging of built-in electric field at a p-n junction by scanning transmission electron microscopy. Sci Rep 5:10040. https://doi.org/10.1038/srep10040

[60] Kaneko H, Homma M, Okada M, Nakamura S, Ikuta N (1976) Fe-Cr-Co ductile magnet with (BH)max?8 MGOe, In: InAIP Conference Proceedings, pp 620–621. https://doi.org/10.1063/1.30486

[61] Sun XY, Xu CY, Zhen L, Lv LX, Yang L (2007) Evolution of modulated structure in Fe–Cr–Co alloy during isothermal ageing with different external magnetic field conditions. J Magn Magn Mater 312:342–346. https://doi.org/10.1016/j.jmmm.2006.10.722

[62] Sugimoto S, Okada M, Homma M (1988) The enhancement of the magnetic properties of Fe-Cr-Co-Mo polycrystalline permanent magnet alloys by cold rolling and annealing. J Appl Phys 63:3707–3709. https://doi.org/10.1063/1.340642

[63] Stelmashok SI, Milyaev IM, Yusupov VS, Milyaev AI (2017) Magnetic and mechanical properties of hard magnetic alloys 30Kh21K3M and 30Kh20K2M2V. Met Sci Heat Treat 58:622–627. https://doi.org/10.1007/s11041-017-0067-3

[64] Belozerov EV, Mushnikov NV, Ivanova GV, Shchegoleva NN, Serikov VV, Kleinerman NM, Vershinin AV, Uimin MA (2012) High-strength magnetically hard Fe-Cr-Co-based alloys with reduced content of chromium and cobalt. Phys Met Metallogr 113:319–325. https://doi.org/10.1134/S0031918X12040023

[65] Altafi M, Mohammad Sharifi E, Ghasemi A (2020) The effect of various heat treatments on the magnetic behavior of the Fe-Cr-Co magnetically hard alloy. J Magn Magn Mater 507:166837. https://doi.org/10.1016/j.jmmm.2020.166837